

Article

Design of $\text{Na}_3\text{MnZr}(\text{PO}_4)_3$ /Carbon Nanofiber Free-Standing Cathodes for Sodium-Ion Batteries with Enhanced Electrochemical Performances through Different Electrospinning Approaches

Debora Maria Conti ¹, Claudia Urru ¹, Giovanna Bruni ¹, Pietro Galinetto ², Benedetta Albini ², Chiara Milanese ¹, Silvia Pisani ³, Vittorio Berbenni ¹ and Doretta Capsoni ^{1,*}

¹ Department of Chemistry, Physical Chemistry Section & C.S.G.I. (Consorzio Interuniversitario per lo Sviluppo dei Sistemi a Grande Interfase), University of Pavia, Via Taramelli 16, 27100 Pavia, Italy; deboramaria.conti01@universitadipavia.it (D.M.C.); claudia.urr01@universitadipavia.it (C.U.); giovanna.bruni@unipv.it (G.B.); chiara.milanese@unipv.it (C.M.); vittorio.berbenni@unipv.it (V.B.)

² Department of Physics, University of Pavia, 27100 Pavia, Italy; pietro.galinetto@unipv.it (P.G.); benedetta.albini@unipv.it (B.A.)

³ Department of Drug Sciences, University of Pavia, Via Taramelli 12, 27100 Pavia, Italy; silvia.pisani@unipv.it

* Correspondence: doretta.capsoni@unipv.it; Tel.: +39-0382-987213

Abstract: The NASICON-structured $\text{Na}_3\text{MnZr}(\text{PO}_4)_3$ compound is a promising high-voltage cathode material for sodium-ion batteries (SIBs). In this study, an easy and scalable electrospinning approach was used to synthesize self-standing cathodes based on $\text{Na}_3\text{MnZr}(\text{PO}_4)_3$ loaded into carbon nanofibers (CNFs). Different strategies were applied to load the active material. All the employed characterization techniques (X-ray powder diffraction (XRPD), scanning electron microscopy (SEM), transmission electron microscopy (TEM), energy-dispersive X-ray spectroscopy (EDS), thermal gravimetric analysis (TGA), and Raman spectroscopy) confirmed the successful loading. Compared to an appropriately prepared tape-cast electrode, $\text{Na}_3\text{MnZr}(\text{PO}_4)_3$ /CNF self-standing cathodes demonstrated an enhanced specific capacity, especially at high C-rates, thanks to the porous conductive carbon nanofiber matrix. Among the strategies applied to load $\text{Na}_3\text{MnZr}(\text{PO}_4)_3$ into the CNFs, the electrospinning (vertical setting) of the polymeric solution containing pre-synthesized $\text{Na}_3\text{MnZr}(\text{PO}_4)_3$ powders resulted effective in obtaining the quantitative loading of the active material and a homogeneous distribution through the sheet thickness. Notably, $\text{Na}_3\text{MnZr}(\text{PO}_4)_3$ aggregates connected to the CNFs, covered their surface, and were also embedded, as demonstrated by TEM and EDS. Compared to the self-standing cathodes prepared with the horizontal setting or dip-drop coating methods, the vertical binder-free electrode exhibited the highest capacity values of 78.2, 55.7, 38.8, 22.2, 16.2, 12.8, 10.3, 9.0, and 8.5 mAh/g at C-rates of 0.05C, 0.1C, 0.2C, 0.5C, 1C, 2C, 5C, 10C, and 20C, respectively, with complete capacity retention at the end of the measurements. It also exhibited a good cycling life, compared to its tape-cast counterpart: it displayed higher capacity retention at 0.2C and 1C, and, after cycling 1000 cycles at 1C, it could be further cycled at 5C, 10C, and 20C.

Keywords: $\text{Na}_3\text{MnZr}(\text{PO}_4)_3$; cathode; sodium-ion batteries; electrospinning; carbon nanofibers; free-standing



Citation: Conti, D.M.; Urru, C.; Bruni, G.; Galinetto, P.; Albini, B.; Milanese, C.; Pisani, S.; Berbenni, V.; Capsoni, D. Design of $\text{Na}_3\text{MnZr}(\text{PO}_4)_3$ /Carbon Nanofiber Free-Standing Cathodes for Sodium-Ion Batteries with Enhanced Electrochemical Performances through Different Electrospinning Approaches. *Molecules* **2024**, *29*, 1885. <https://doi.org/10.3390/molecules29081885>

Academic Editors: Yuanyuan Zhu and Yanmin Jia

Received: 18 March 2024

Revised: 12 April 2024

Accepted: 18 April 2024

Published: 20 April 2024



Copyright: © 2024 by the authors. Licensee MDPI, Basel, Switzerland. This article is an open access article distributed under the terms and conditions of the Creative Commons Attribution (CC BY) license (<https://creativecommons.org/licenses/by/4.0/>).

1. Introduction

In a world rapidly moving towards renewable energy sources for limiting global climate change and promoting the transition to less carbon-intensive and more sustainable energy systems, the development of efficient energy storage devices to integrate intermittent energy production is a key issue [1,2]. Undoubtedly, rechargeable batteries have been regarded as promising energy storage systems, and, among them, lithium-ion batteries (LIBs) occupy a pivotal position, thanks to their high energy density, operating voltage,

specific capacity, and long cycle life [3–7]. However, the non-ubiquitous distribution of lithium resources and their depletion inevitably cause price increases and pose concerns for large-scale applications [8–13]: for these reasons, alternative energy storage systems involving less critical elements need to be explored. Sodium-ion batteries (SIBs) seem to be a valuable choice, as sodium is a ubiquitous, abundant, and low-cost element [14,15]. Notably, sodium and lithium present comparable chemical and physical properties and a similar intercalation chemistry. Despite these appealing features and the progress recently achieved, several shortcomings still need to be addressed to develop SIBs with high energy and power densities, good lifespans, and fast sodium-ion diffusion and kinetics [16]. Among the battery components, cathodes play a key role, and the development of new and performant cathode materials is necessary to address the abovementioned drawbacks. Layered/tunneled transition metal oxides have been widely investigated as cathodes for SIBs, but the volume changes upon sodiation/desodiation and phase instabilities pose concerns about their application [17–22]. Prussian blue analogues are promising for their low cost, easy synthesis, and fast Na^+ migration within the crystal network [23–27]. Polyanionic compounds were revealed to be suitable cathode materials, as they offer a robust three-dimensional polyanionic framework with tunnels for ion migration [28–31]. Among them, NASICON-structured cathodes have been widely investigated, thanks to the possibility to tune electrochemical performance by varying the transition metal ion. Compounds such as $\text{Na}_3\text{V}_2(\text{PO}_4)_3$, $\text{Na}_3\text{Cr}_2(\text{PO}_4)_3$, and $\text{Na}_3\text{Fe}_2(\text{PO}_4)_3$ were investigated and modified by carbon coating or doping to improve their low electronic conductivity [32–35]. Recently, research efforts have focused on NASICON-type mixed-transition metal phosphates, such as $\text{Na}_3\text{Mn}^{2+}\text{M}(\text{PO}_4)_3$ (M = tetravalent metal ion), in which high discharge voltages are achieved thanks to the reversible redox processes involving both $\text{Mn}^{4+}/\text{Mn}^{3+}$ and $\text{Mn}^{3+}/\text{Mn}^{2+}$ couples [36–40]. Among these phosphates, the $\text{Na}_3\text{MnZr}(\text{PO}_4)_3$ cathode exhibits superior electrochemical performance [38,41]: it provides high voltage plateaus at 4.1 V and 3.5 V, corresponding to the reversible extraction of two Na^+ ions with small changes in the cell volume. $\text{Na}_3\text{MnZr}(\text{PO}_4)_3$ crystallizes in the rhombohedral $R\bar{3}c$ space group with lattice parameters $a = 8.988 \text{ \AA}$ and $c = 22.598 \text{ \AA}$. Mn and Zr randomly occupy the octahedral sites of the NASICON structure. The Mn/Zr octahedra connect via oxygen to the PO_4 tetrahedra to form a 3D network with three interstitial sites accessible for Na^+ ions: Na(1), Na(2), and Na(3). These sites are partially occupied, and the Coulombic repulsion of the Na^+ ions in Na(1) and Na(2) causes the displacement of Na^+ ions from the Na(1) to Na(3) site. The sodiation and desodiation processes involve the Na(2) site. Gao and coworkers [38] reported a detailed investigation of the intercalation/deintercalation mechanism and demonstrated the suppression of the Jahn–Teller distortion of Mn^{3+} in $\text{Na}_3\text{MnZr}(\text{PO}_4)_3$ compared to other Mn-based phosphates. Ma and coworkers [41] reported that the electrochemical performance of the $\text{Na}_3\text{MnZr}(\text{PO}_4)_3$ cathode can be further improved by preparing $\text{Na}_3\text{MnZr}(\text{PO}_4)_3$ microspheres with an embedded dual-carbon-based material (amorphous carbon and reduced graphene oxide).

In recent years, carbon nanofibers (CNFs) have been successfully employed in different areas such as energy [42], biomedicine [43,44], gas storage/separation [45,46], adsorption [47,48], and catalysis [49]. In the energy field, CNFs are well employed in LIBs and SIBs as anodes [50] or as the conductive filler and matrix of electrode materials [51–56]. CNFs are good electronic conductors and display a high surface area. They are easily synthesized by electrospinning and the obtained non-woven sheets possess a desirable porosity, favoring good electrolyte permeation and allowing the volume changes occurring during the sodiation/desodiation processes. Moreover, thanks to their good electronic conductivity and mechanical properties, CNFs are suitable for fabricating free-standing electrodes, avoiding the employment of Al foils as active material supports and current collectors. The active material can be loaded into CNFs by different approaches: (i) it is pre-synthesized and then dispersed in the polymeric solution to be electrospun, and, subsequently, the obtained sheet undergoes a carbonization process [54]; (ii) a solution containing the precursors of the active material is added to the polymeric solution to be

electrospun, and the obtained sheets are thermally treated to carbonize, leading to the formation of the final product [51–53]; and (iii) the active materials' precursor solution is added by a dip-drop method to pre-synthesized CNFs, and the soaked sheet is thermally treated to synthesize the active material into CNFs [55,56].

In this paper, we prepared and characterized, for the first time in the literature to our knowledge, $\text{Na}_3\text{MnZr}(\text{PO}_4)_3/\text{CNF}$ self-standing cathodes, and we tested their electrochemical performances for applications in SIBs. $\text{Na}_3\text{MnZr}(\text{PO}_4)_3$ was chosen, as it is an appealing high-voltage cathode material compared to other mixed-transition metal phosphates [38,40,41]. CNFs are good electronic conductors; the electrolyte easily permeates their porous structure, and electrolyte–active material contact is facilitated. Based on the aforementioned CNF features, improved electrochemical performance with respect to conventional tape-cast cathodes is envisaged especially at high C-rates ($\geq 10\text{C}$), where the required fast ion diffusion is invalidated in packed materials [57,58]. The self-standing cathodes were prepared by electrospinning using both the dip-drop method on pre-electrospun CNFs and the dispersion of pre-synthesized $\text{Na}_3\text{MnZr}(\text{PO}_4)_3$ in the polymeric solution to be electrospun. Different electrospinning settings were also applied (horizontal and vertical settings). The obtained composites were characterized by several techniques to investigate structure, morphology, composition, and $\text{Na}_3\text{MnZr}(\text{PO}_4)_3$ distribution into the CNFs. The electrochemical performance of the free-standing electrodes was evaluated and compared to that of a conventional tape-cast cathode (70% active material), appositely prepared. We expected to obtain improved electrochemical performance for the self-standing cathodes, especially at high C-rates. Based on the physico-chemical features and electrochemical results, we could also identify the most efficient synthetic approach to prepare binder-free electrodes.

2. Results

2.1. *p*-MnZr and MnZr/CNF Characterization

Pristine $\text{Na}_3\text{MnZr}(\text{PO}_4)_3$ powder was synthesized via the sol-gel method [38] and used as the active material source in preparing both tape-cast electrode and some of the free-standing cathodes. Two different approaches were applied to prepare the self-standing electrodes, differing on the method employed to load the active material onto the CNFs: (i) dip-drop coating of the $\text{Na}_3\text{MnZr}(\text{PO}_4)_3$ precursors onto electrospun CNFs sheets, followed by thermal treatments to synthesize the active material, or (ii) electrospinning the dispersion of pristine $\text{Na}_3\text{MnZr}(\text{PO}_4)_3$ powder synthesized via sol-gel into PAN in a *N,N*-dimethylacetamide (DMAc) solution. In the latter case, two different $\text{Na}_3\text{MnZr}(\text{PO}_4)_3$ amounts (10 and 30 wt%) and two electrospinning settings (horizontal and vertical) were investigated. Also, pure CNFs were prepared for comparison. A scheme of the samples' synthesis is shown in Figure 1, and details are reported in Section 3.2. The prepared samples and their alphanumeric codes are listed in Table 1.

In Figure 2, the XRPD patterns of CNF, *p*-MnZr, *dd*-MnZr/CNF, *h*-10%MnZr/CNF, *h*-30%MnZr/CNF, and *v*-30%MnZr/CNF are shown. For the CNF sample, a broad band centered at a 2-theta value of about 25° is detected, as expected for amorphous components. The *p*-MnZr sample displays the peaks pertinent to the NASICON-type $\text{Na}_3\text{MnZr}(\text{PO}_4)_3$ compound ($R\bar{3}c$ space group) deposited in the JCPDS database (PDF# 041-0504). The diffraction data are well explained by the literature structure given by Gao and co-workers [38], as demonstrated by the Rietveld refinement results reported in Table S1 and the graphical comparison in Figure S1. No extra peaks due to Mn and Zr long-range ordering are detected, and the random distribution of the transition metal ions on the octahedral site of the NASICON framework is confirmed [59,60]. For the MnZr/CNFs samples, both the broad band typical of the amorphous component and the reflections of the $\text{Na}_3\text{MnZr}(\text{PO}_4)_3$ NASICON structure are observed, independently of the deposition method. The self-standing cathode obtained by the dip-drop approach is impurity-free, while those prepared by dispersing the active material into the PAN solution display a weak peak at 2-theta of about 32° : this signal is explained by a small amount of $\text{MnZr}_4(\text{PO}_4)_6$ phase (PDF# 045-0016), possibly

formed during the further thermal treatment at 750 °C for the carbonization process. The Rietveld refinement results for the MnZr/CNFs samples are reported in Table S1, and the graphical comparisons are shown in Figure S2. The crystalline component of the diffraction patterns is well explained by the $\text{Na}_3\text{MnZr}(\text{PO}_4)_3$ phase. Notably, the c lattice parameter increases and a decreases compared to the pristine $\text{Na}_3\text{MnZr}(\text{PO}_4)_3$ powder. This leads to a slight cell volume decrease and a c/a ratio increase (See Table S1). The crystallite size is slightly increased in the self-standing cathodes obtained by the dispersion approach, and it is consistent with the prolonged thermal treatment at 750 °C for the additional carbonization process, not required in the pristine and dip-drop synthesis routes.

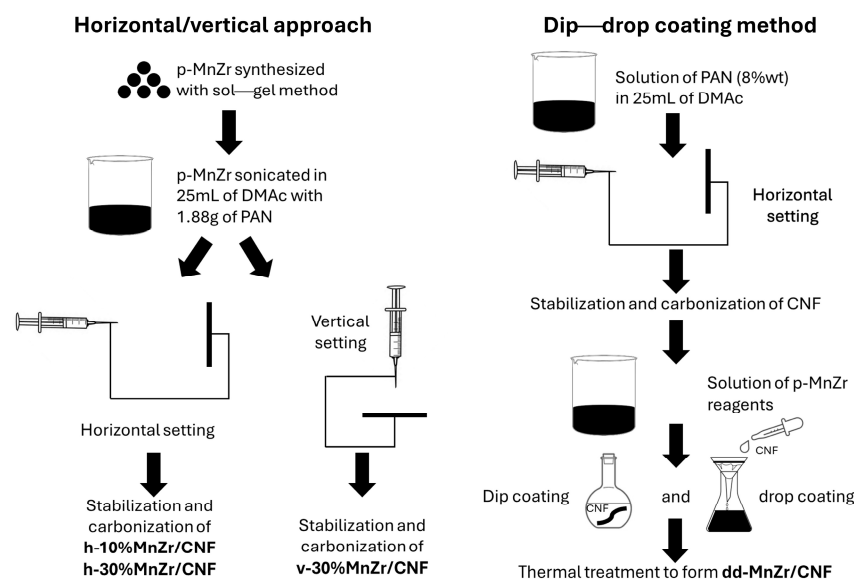


Figure 1. A scheme of the samples' synthesis.

Table 1. List and preparation details of the investigated samples.

CODE	SAMPLE	DETAILS
CNF	Pure carbon nanofibers	Electrospinning Setting: horizontal
p-MnZr	Pristine $\text{Na}_3\text{MnZr}(\text{PO}_4)_3$ powder	Sol-gel route
dd-MnZr/CNF	Self-standing cathode 33 wt% active material (from TGA)	Electrospinning Dip-drop method Setting: horizontal
h-10%MnZr/CNF	Self-standing cathode 10 wt% active material (from synthesis)	Electrospinning Active material dispersion Setting: horizontal
h-30%MnZr/CNF	Self-standing cathode 30 wt% active material (from synthesis)	Electrospinning Active material dispersion Setting: horizontal
v-30%MnZr/CNF	Self-standing cathode 30 wt% active material (from synthesis)	Electrospinning Active material dispersion Setting: vertical

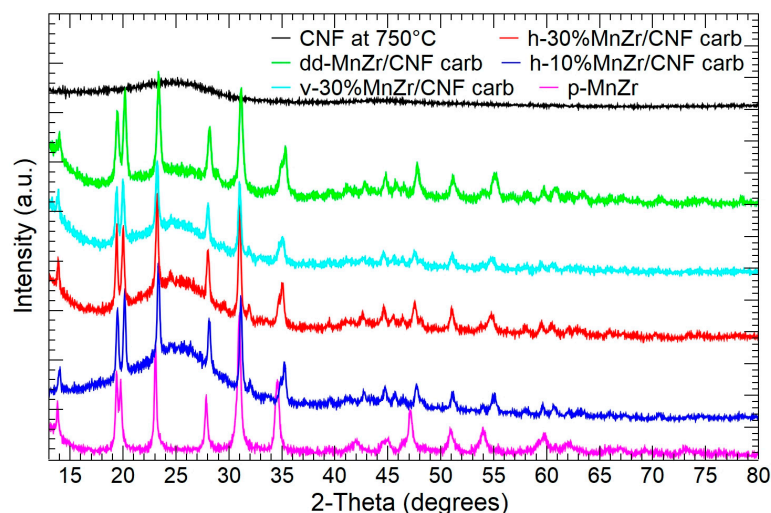


Figure 2. XRPD patterns of CNFs, pristine $\text{Na}_3\text{MnZr}(\text{PO}_4)_3$ powder, and self-standing cathodes.

To analyze the phase formation and composition of the composite samples, we also employed micro-Raman spectroscopy. The Raman spectra of the pristine $\text{Na}_3\text{MnZr}(\text{PO}_4)_3$ and MnZr/CNFs samples are shown in Figure 3. In the case of highly diffusive powders, it is important to note that micro-Raman sampling is strongly effective in surface layers.

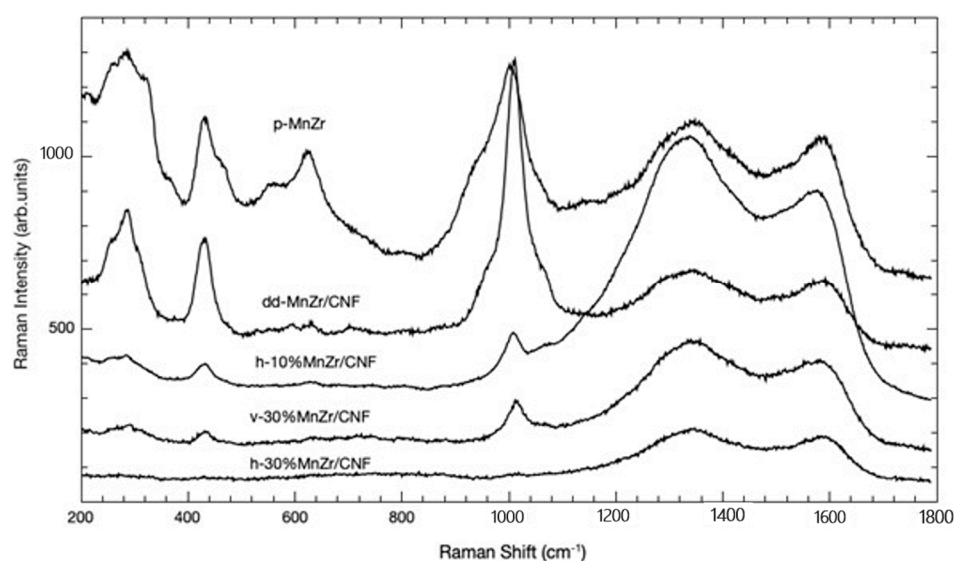


Figure 3. Raman spectra of p-MnZr, h-10%MnZr/CNF, h-30%MnZr/CNF, v-30%MnZr/CNF, and dd-MnZr/CNF samples.

In all the cases, we can distinguish two different spectral regions: the first, in the range $200\text{--}1100\text{ cm}^{-1}$, presents Raman features ascribed to the active material [61], while the second, in the range $1100\text{--}1800\text{ cm}^{-1}$, presents the typical fingerprints of carbon-based structures, with the well-known D and G bands [62].

In the first spectral region, the typical spectrum of $\text{Na}_3\text{MnZr}(\text{PO}_4)_3$ is observed for the pristine sample. The strong signal at around 1000 cm^{-1} is due to the overlapping of the Raman activity associated with PO_4 symmetric (ν_1) and asymmetric (ν_3) stretching vibrations. At lower energies, different Raman activities can be present. The strong signal at around 430 cm^{-1} could be due to symmetric (ν_2) bending vibrations of the PO_4 unit, with the corresponding asymmetric (ν_4) bending mode responsible for the lower-intensity signals around 540 cm^{-1} . The bands observed in the $350\text{--}330\text{ cm}^{-1}$ range could be instead associated with metal–oxygen vibrations, while bands below 250 cm^{-1} are usually

attributed to lattice vibrations. Even for the pristine sample, typical carbon-related Raman features are observed, possibly due to the carbon coating.

Moreover, we can observe that the active material's Raman fingerprint is clearly visible for the dd-MnZr/CNF sample, while it is attenuated for all the other ones. This is due to the different preparation methods leading to different in-depth profiles of the active material, as confirmed by the EDS analysis reported below.

Concerning the carbon-related features, i.e., the bands at 1333 and 1586 cm^{-1} , the former related to the disordered carbon, the latter to the G band, we observe an almost constant ratio between their intensities except for the h-10%MnZr/CNF sample, where the disorder, i.e., a greater I_D/I_G ratio, is more pronounced.

Figure 4 shows the SEM and TEM images of the pristine $\text{Na}_3\text{MnZr}(\text{PO}_4)_3$ powder. The SEM image shows large aggregates composed by nanometric sub-particles with a homogeneous morphology. The grains' surface is irregular but defined. The TEM micrograph (Figure 4b) of the p-MnZr sample confirms the presence of aggregates of nanometric particles covered by a homogeneous carbon coating resulting from the citric acid decomposition occurred during sol-gel synthesis.

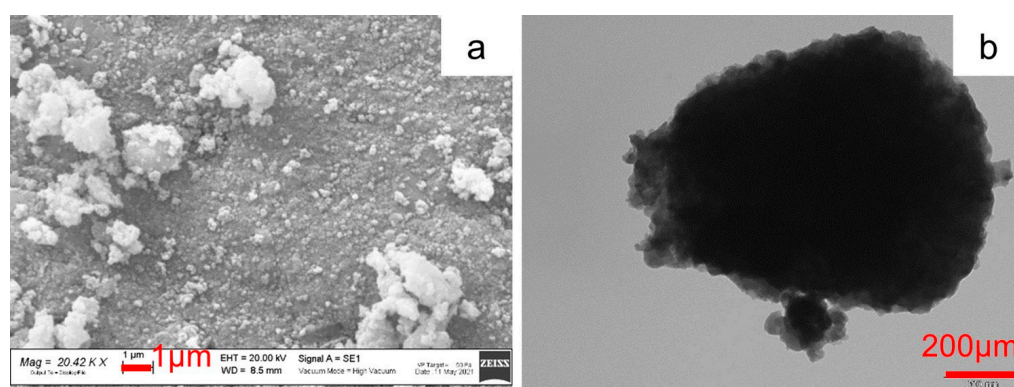


Figure 4. SEM and TEM images of $\text{Na}_3\text{MnZr}(\text{PO}_4)_3$ powder: (a) 20.42 kX and (b) 100 kX.

Figure 5 shows the SEM images of self-standing cathodes. For each sample, both the surface and the cross-section are investigated. All the self-standing electrodes are characterized by a matrix of non-woven carbon nanofibers, which hosts the $\text{Na}_3\text{MnZr}(\text{PO}_4)_3$ aggregates of a micrometric size. Also, the carbon nanofibers display variable dimensions, averaging about 250 nm for the samples prepared dispersing the active material in the PAN solution before electrospinning and larger in the dip-drop sample (about 700 nm). The cross-section images put into evidence that a higher thickness (about 150 nm) is obtained for the 30 wt% samples, independently of the deposition setting. The sheets seem more compact and structured for the h-10%MnZr/CNF, h-30%MnZr/CNF, and v-30%MnZr/CNF samples and fluffier in the case of the dip-drop one.

Figure 6 shows the TEM images of self-standing samples, which confirm the presence of active material agglomerates in CNFs, as evidenced by the SEM analysis. The aggregates are formed by sub-particles of about 20–40 nm, whose size compares to that evaluated by XRPD analysis (Table S1). Interestingly, in the samples prepared by the dispersion of pristine $\text{Na}_3\text{MnZr}(\text{PO}_4)_3$ into the polymeric solution to be electrospun, the active material covers parts of the CNF surface but is also embedded into nanofibers; the latter feature is particularly evident in the v-30%MnZr/CNF sample. Differently, the agglomerates reside mainly on the CNFs surface and between them in the case of the dip-drop approach. This is consistent with the different synthetic route, in which the active material is formed in situ on carbonized electrospun nanofibers.

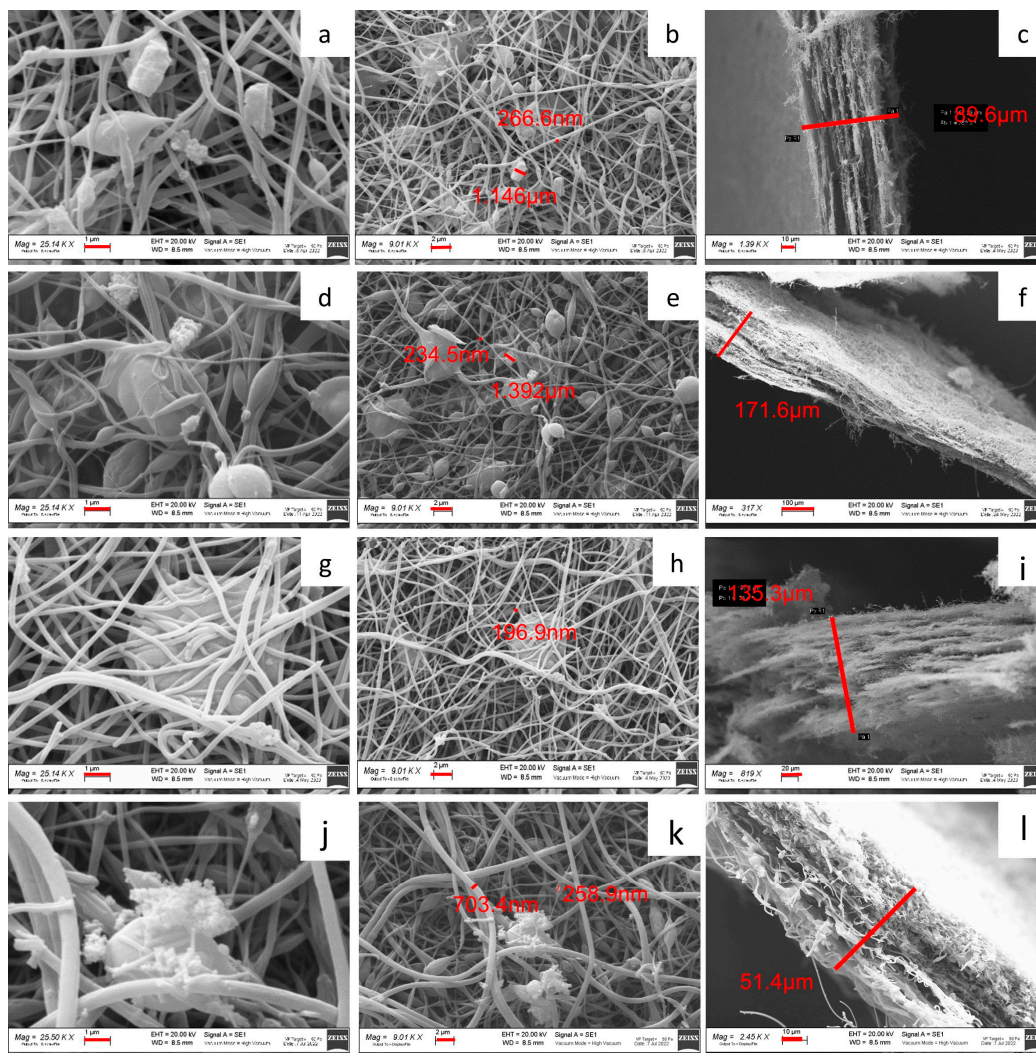


Figure 5. SEM images of h-10%MnZr/CNF (a,b) surface and (c) cross-section; h-30%MnZr/CNF (d,e) surface and (f) cross-section; v-30%MnZr/CNF (g,h) surface and (i) cross-section; and dd-MnZr/CNF (j,k) surface and (l) cross-section.

To evaluate the $\text{Na}_3\text{MnZr}(\text{PO}_4)_3$ distribution on the surface and within the cross-section of the MnZr/CNF self-standing electrodes, an EDS analysis was performed. For each sample, a surface and a cross-section portion were selected, and the distribution maps of the Na, Mn, Zr, and P elements were evaluated. The results are shown in Figures 7–10 for the h-10%MnZr/CNF, h-30%MnZr/CNF, v-30%MnZr/CNF, and dd-MnZr/CNF self-standing cathodes. In the case of the active material loaded by dispersion into the polymeric solution, the EDS analysis demonstrated that the agglomerates dispersed into and within the CNFs corresponded to $\text{Na}_3\text{MnZr}(\text{PO}_4)_3$ composition. They were homogeneously distributed on the sample surface and along the sheet thickness too (Figures 7–9). For the dd-MnZr/CNF sample (Figure 10), again the $\text{Na}_3\text{MnZr}(\text{PO}_4)_3$ agglomerates were detected on the surface and in the cross-section, but their distribution along the sheet thickness was non-homogeneous, and the active material preferentially resided on the external edges. This justified the clearly visible Raman fingerprint of $\text{Na}_3\text{MnZr}(\text{PO}_4)_3$ in the dd-MnZr/CNF composite compared to the other self-standing cathodes and was consistent with the dip–drop synthetic approach used to load the active material: the permeation of the precursors' solution into the inner part of the pre-synthesized CNF sheets was less effective. The different concentration of the active material along the sheet may have influenced the electrochemical performance of the self-standing electrode. The atomic

percentage of the Na, Mn, and P elements and their ratio were evaluated by EDS elemental analysis: independently of the self-standing MnZr/CNF cathodes, the Na:Mn:P mole ratio was close to 3:1:3, as expected from the compound's stoichiometry.

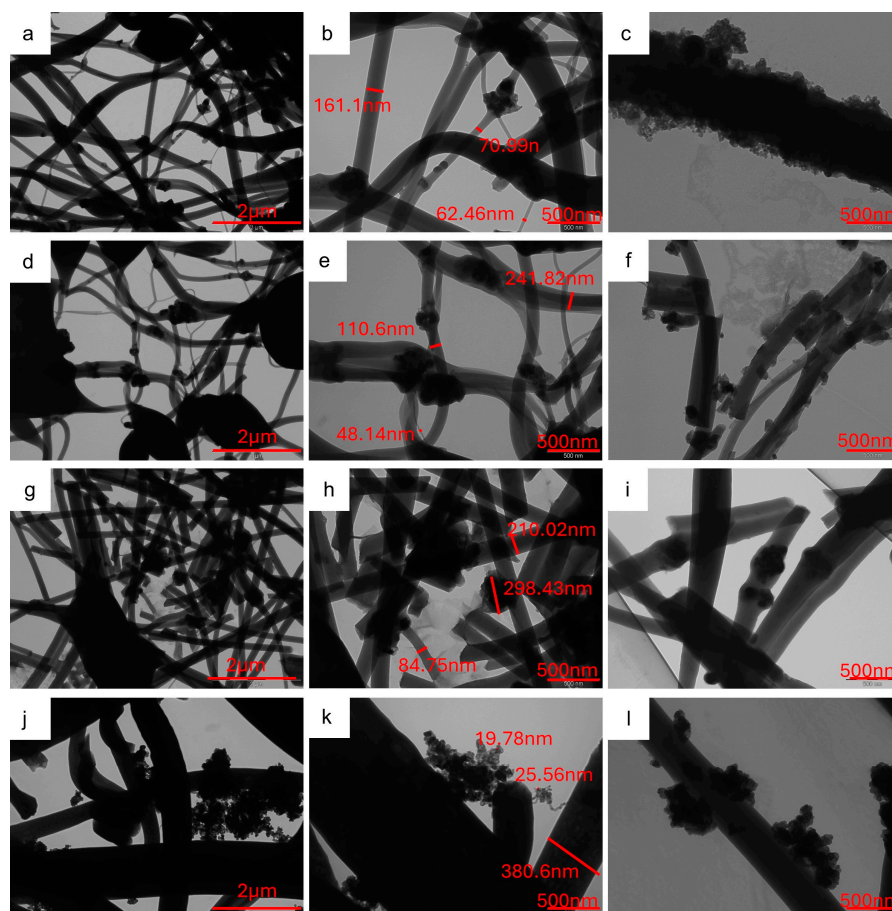


Figure 6. TEM images at different magnifications (20 kX e 50 kX) of (a–c) h-10%MnZr/CNF, (d–f) h-30%MnZr/CNF, (g–i) v-30%MnZr/CNF, and (j–l) dd-MnZr/CNF samples.

The thermogravimetric data were used to evaluate the effective amount of the $\text{Na}_3\text{MnZr}(\text{PO}_4)_3$ active material present in the self-standing cathodes. The thermal behavior of the pristine $\text{Na}_3\text{MnZr}(\text{PO}_4)_3$ powder was also investigated.

The thermogravimetric curves of the p-MnTi, h-10%MnZr/CNF, h-30%MnZr/CNF, v-30%MnZr/CNF, and dd-MnZr/CNF samples are shown in Figure 11. For the p-MnZr sample (black line), a small mass loss due to the release of adsorbed water was detected below 100 °C, while the second mass loss of 5.13% occurring in the temperature range 400–650 °C was attributed to the combustion of the carbon coating (source: citric acid used in sol–gel synthesis).

The h-10%MnZr/CNF (blue line), h-30%MnZr/CNF (red line), v-30%MnZr/CNF (green line), and dd-MnZr/CNF TGA curves displayed a similar thermal behavior. As for the p-MnZr sample, the first mass loss below 100 °C was attributed to the adsorbed water release. The second mass loss in the 400–650 °C temperature range was again due to the combustion of the carbonaceous component present as both the carbon coating and the carbon nanofibers. So, it was expected that this mass loss would be higher for MnZr/CNFs than the p-MnZr sample. The residual mass values reached by each self-standing cathode are reported in Table 2. In the case of the h-10%MnZr/CNF self-standing electrode, the obtained value well matched the synthesis one. On the contrary, for h-30%MnZr/CNF, the value was lower. This may depend on the horizontal experimental setting used for the deposition: we noted the partial settling of particles agglomerates in the syringe. To achieve

the 30 wt% loading, the vertical experimental setting was used to prepare the self-standing cathode. Indeed, for the v-30%MnZr/CNF sample, the mass loading matched the synthesis value. The highest active material loading was obtained for the dd-MnZr/CNF sample by electrospinning the polymeric solution containing the $\text{Na}_3\text{MnZr}(\text{PO}_4)_3$ precursors.

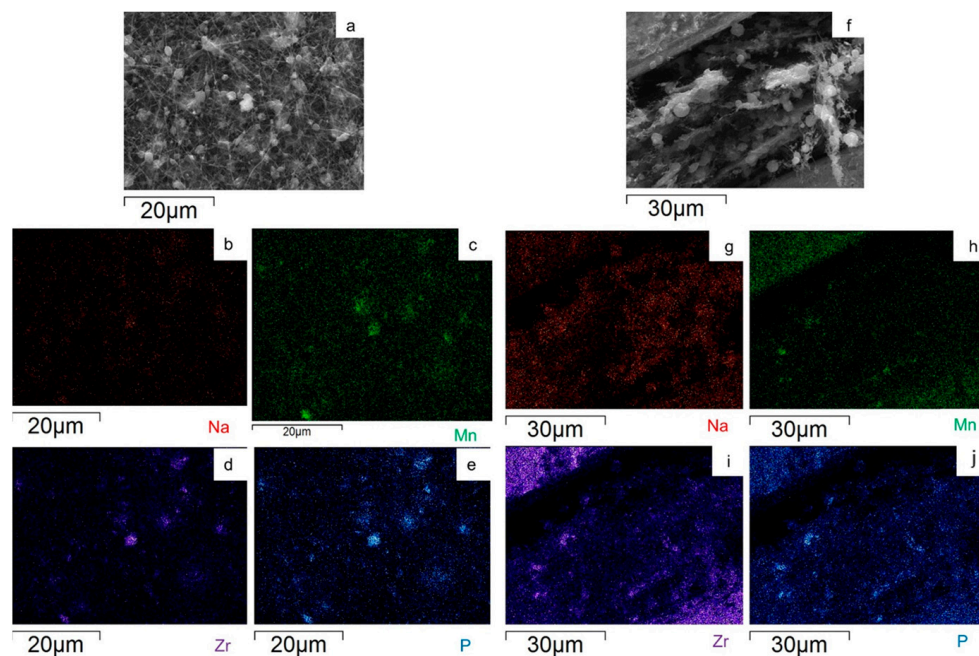


Figure 7. SEM image and EDS maps of the different elements for the h-10%MnZr/CNF (a–e) surface and (f–j) its cross-section.

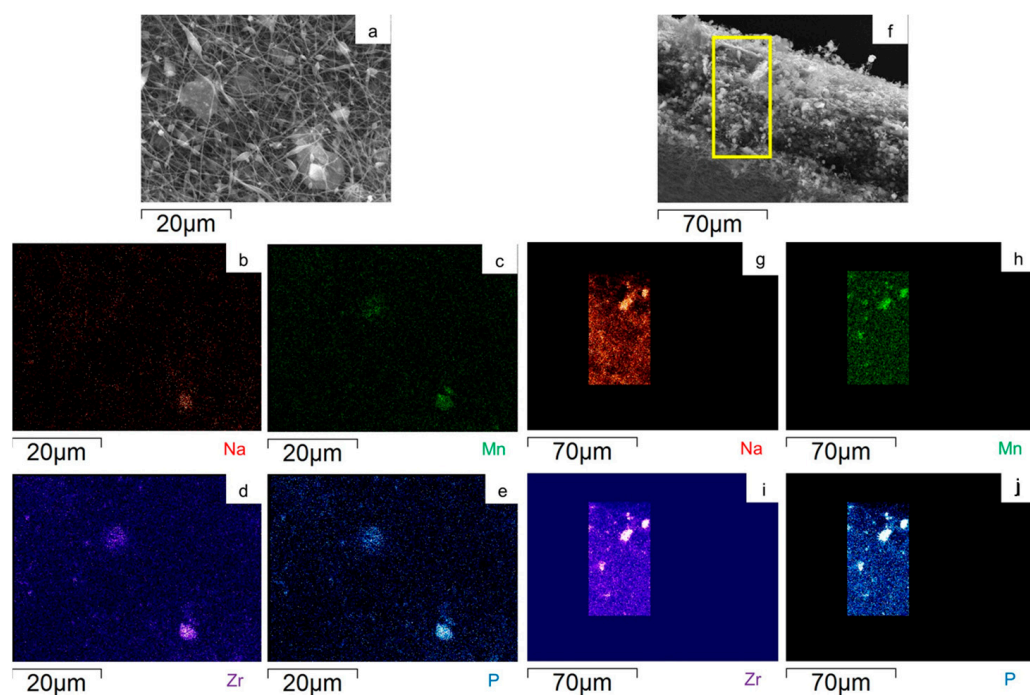


Figure 8. SEM image and EDS maps of the different elements for the h-30%MnZr/CNF (a–e) surface and (f–j) its cross-section. The yellow frame indicates the mapped portion.

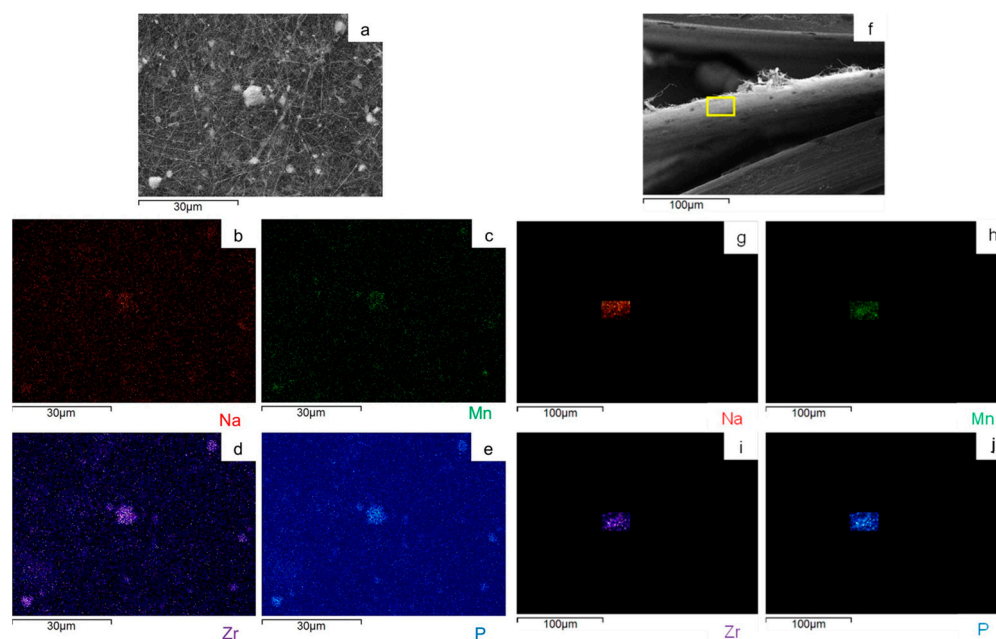


Figure 9. SEM image and EDS maps of the different elements for the v-30%MnZr/CNF (a–e) surface and (f–j) its cross-section. The yellow frame indicates the mapped portion.

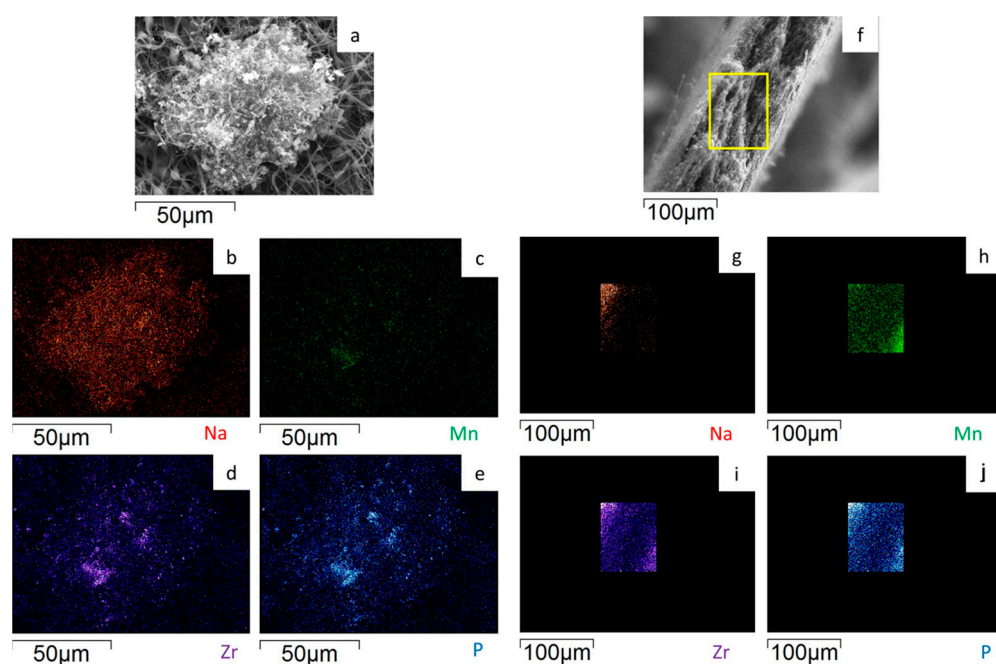


Figure 10. SEM image and EDS maps of the different elements for the dd-MnZr/CNF (a–e) surface and (f–j) its cross-section. The yellow frame indicates the mapped portion.

From the values of the electrode residual masses for the v-30%MnZr/CNF and dd-MnZr/CNF samples we evaluated an active material loading of about 1.9 mg/cm^2 , which is consistent with the literature values of self-standing electrodes [56,63].

The characterization results put into evidence the analogies/differences of the self-standing cathodes prepared by different synthetic approaches and settings. In all cases, the active material was successfully loaded into the carbon nanofibers. The direct dispersion of pre-synthesized $\text{Na}_3\text{MnZr}(\text{PO}_4)_3$ powder into the polymeric solution before electrospinning seems a promising and feasible route for loading the active material. It was homogeneously dispersed both into and within CNFs. The effective loading was quantitative when using

the vertical setting, which prevented the possible settling of the powder before the needle was reached. The dip-drop coating of the active material precursor solution onto electro-spun carbon nanofibers allowed the load of the highest $\text{Na}_3\text{MnZr}(\text{PO}_4)_3$ amount, but the product mainly resided on the CNF sheet surface and did not distribute homogeneously along the sheet thickness.

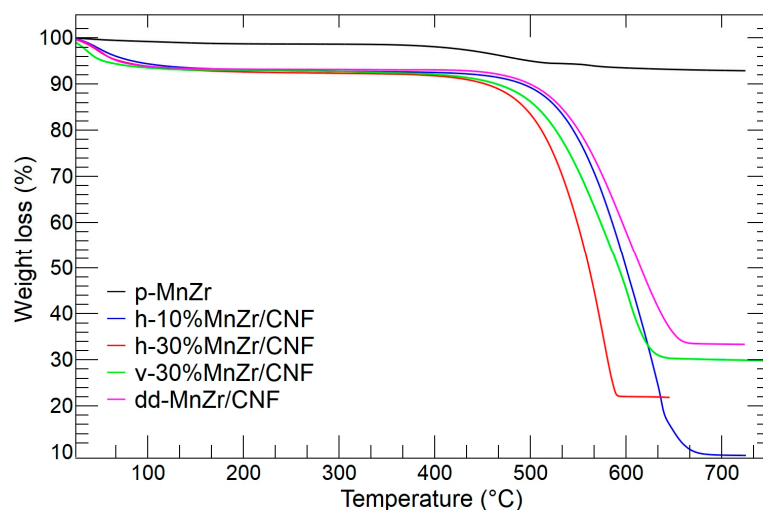


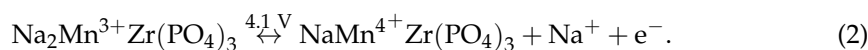
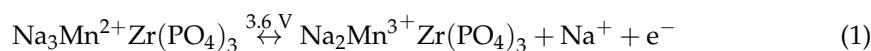
Figure 11. TGA analysis of p-MnZr (black), h-10%MnZr/CNF (blue), h-30%MnZr/CNF (red) v-30%MnZr/CNF (green), and dd-MnZr/CNF (purple) samples.

Table 2. Residual mass values of the self-standing cathodes evaluated by TGA analysis.

SAMPLE	RESIDUAL MASS (wt%)
h-10%MnZr/CNF	9.3
h-30%MnZr/CNF	21.8
v-30%MnZr/CNF	29.8
dd-MnZr/CNF	33.3

2.2. p-MnZr and MnZr/CNF Electrochemical Characterization

The cyclic voltammetry of the $\text{Na}_3\text{MnZr}(\text{PO}_4)_3$ material presented two redox peaks at 3.6 V and 4.1 V related to the $\text{Mn}^{2+}/\text{Mn}^{3+}$ and $\text{Mn}^{3+}/\text{Mn}^{4+}$ redox couples, respectively [38]. They indicated the reversible extraction/insertion of two Na^+ ions involving the two-phase redox processes reported in Equations (1) and (2) [38,41]:



The presence of Zr^{4+} was only necessary to unlock the rare $\text{Mn}^{3+}/\text{Mn}^{4+}$ redox reaction useful to produce a high-voltage cathode for sodium-ion batteries [64].

Gao and coworkers [38] reported a deep investigation of the desodiation process based on ex situ X-ray diffraction structural analysis and density functional theory calculations. In the aforementioned process, the Na^+ extraction mainly involves $\text{MnO}_6\text{-Na(2)-ZrO}_6$ sites leaving $\text{MnO}_6\text{-Na(2)-MnO}_6$ and $\text{MnO}_6\text{-Na(1)-MnO}_6$ occupied. During desodiation, the $\text{ZrO}_6\text{-Na(1)-ZrO}_6$ occupation increases and the Na(2) vacancies promote Na(1) displacement to the Na(3) site. The latter process leads to completely occupied Na(1) sites and unoccupied Na(2) ones.

Figure S3 reports the cyclic voltammetry and charge/discharge curves for the p-MnZr slurry and MnZr/CNF self-standing electrodes. The p-MnZr slurry electrode data

(Figure S3a,b) well compared to the literature ones [38]: the two redox peaks of $\text{Mn}^{2+}/\text{Mn}^{3+}$ and $\text{Mn}^{3+}/\text{Mn}^{4+}$ were detected at 3.61 V/3.45 V and 4.19 V/4.12 V, respectively. The small ΔV values between the cathodic and anodic peaks (16 mV for $\text{Mn}^{2+}/\text{Mn}^{3+}$ and 7 mV for $\text{Mn}^{3+}/\text{Mn}^{4+}$) indicated a very small polarization phenomenon. The current intensity was higher than 0.05 A/g and lower than -0.03 A/g for the anodic and cathodic peaks, respectively. The two redox phenomena were also confirmed by the two plateaus detected at 4.2 V and 3.5 V in the charge/discharge curves.

In the case of the self-standing cathodes, it was difficult to individuate the manganese redox peaks, as they were very faint. This may have depended on the active material amount, which was lower than that used in the tape-cast cathode. Only in the v-30%MnZr/CNF sample, the weak cathodic peaks at 3.44 V and 4.05 V were detected and confirmed by the presence of the small plateau of $\text{Mn}^{3+}/\text{Mn}^{4+}$ at about 4.1 V in the charge/discharge curves (Figure S3g,h). We recall that, among the cathodes prepared by the dispersion of pre-synthesized $\text{Na}_3\text{MnZr}(\text{PO}_4)_3$, the v-30%MnZr/CNF sample had the highest active material loading (29.8 wt%). For the dd-MnZr/CNF cathode, a comparable $\text{Na}_3\text{MnZr}(\text{PO}_4)_3$ amount (33.0 wt%) was detected, but the active material was not embedded into the CNFs and non-homogeneously dispersed along the CNFs' thickness, as demonstrated by the TEM and EDS analyses: this may have affected the electrochemical performance.

Figure 12 shows the charge/discharge cycles at different C-rates for the slurry and for the MnZr/CNF self-standing cathodes. The tape-cast electrode showed an initial charge and discharge capacity of 105.88 and 67.21 mAh/g, respectively (Figure 12a). The initial capacity loss was typical of the NASICON-structured cathodes containing Zr^{4+} or Ti^{4+} or Al^{3+} , which presented a voltage hysteresis of $\text{Al}^{3+} < \text{Ti}^{4+} < \text{Zr}^{4+}$ [64]. Average discharge capacities of 58.62, 34.61, 21.19, 13.27, 9.01, 5.87, and 3.01 Ah/g at 0.05C, 0.1C, 0.2C, 0.5C, 1C, 2C, and 5C were obtained, respectively. The cell did not completely recover the capacity at the end of the measurement (a capacity of 24.18 mAh/g was reached at 0.05C), and the Coulombic efficiency (CE%) was $\geq 93\%$.

The h-10%MnZr/CNF cathode exhibited an initial charge and discharge capacity of 40.1 and 70.7 mAh/g, respectively (Figure 12b), with a discharge capacity which reached a value of 46.9 mAh/g in the second cycle. We obtained average discharge capacities of 48.6, 19.0, 17.0, 13.1, 11.0, 8.8, 5.9, 3.9, and 2.7 mAh/g at 0.05C, 0.1C, 0.2C, 0.5C, 1C, 2C, 5C, 10C, and 20C, respectively, and a Coulombic efficiency $\geq 95\%$. Contrary to the slurry electrode, the self-standing h-10%MnZr/CNF cathode first exhibited a lower loss capacity as the C-rate increased and, secondly, worked at C-rates higher than 5C and completely recovered the initial capacity at the end of the measurement. Indeed, the 10% self-standing cathode displayed capacity values at 10C comparable to those obtained for the p-MnZr slurry at 5C and a better Coulombic efficiency, which confirmed a better reversibility of the charge and discharge process.

Improved electrochemical performance was obtained for the h-30%MnZr/CNF sample (Figure 12c), which displayed an initial charge and discharge capacity of 83.9 mAh/g and 83.4 mAh/g, respectively. In this case, the initial capacity loss after the first cycle was not detected, and a Coulombic efficiency $\geq 97\%$ was reached, but the capacity was not completely recovered at the end of the measurement (capacity of 45.2 mAh/g). The average discharge capacities of 53.6, 27.6, 22.5, 11.4, 8.5, 5.8, 3.6, 2.7, and 2.1 mAh/g were obtained at 0.05C, 0.1C, 0.2C, 0.5C, 1C, 2C, 5C, 10C, and 20C, respectively. These discharge capacity values were higher than the ones reported for the h-10%MnZr/CNF sample at 0.05C, 0.1C, and 0.2C. This was probably due to the higher amount of p-MnZr powder loaded into the CNF sheets (21.8 wt%).

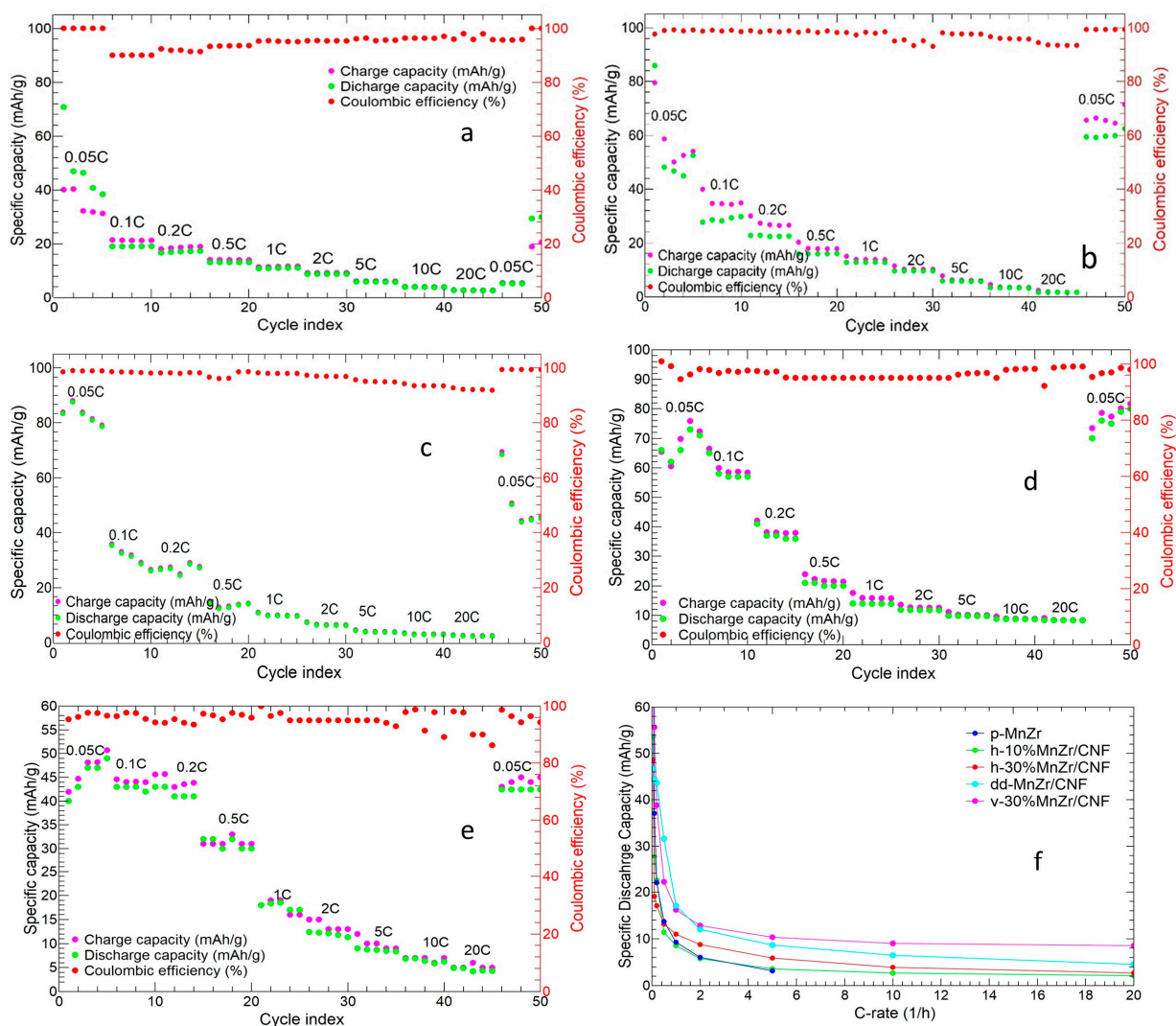


Figure 12. Charge/discharge cycles at different C-rates of (a) p-MnZr, (b) h-10%MnZr/CNF, (c) h-30%MnZr/CNF, (d) v-30%MnZr/CNF, and (e) dd-MnZr/CNF; (f) comparison of average discharge capacity values for all the samples at different C-rates.

Figure 12d shows the charge and discharge cycles at different C-rate for the v-30%MnZr/CNF sample. It exhibited an initial charge and discharge capacity of 65.4 mAh/g and 100.9 mAh/g, respectively, and the discharge value approached the theoretical one (107 mAh/g) [38]. As for h-30%MnZr/CNF, no initial discharge capacity loss was detected, and the sample completely recovered the initial capacity at the end of the measurement with a Coulombic efficiency $\geq 96\%$. The average values of discharge capacity at 0.05C, 0.1C, 0.2C, 0.5C, 1C, 2C, 5C, 10C, and 20C were 78.2, 55.7, 38.8, 22.2, 16.2, 12.8, 10.3, 9.0, and 8.5 mAh/g, respectively. These values were higher at each C-rate than those for the h-10%MnZr/CNF and h-30%MnZr/CNF samples thanks to the higher amount of p-MnZr powder loaded into the CNF sheets.

Finally, the charge/discharge cycles at different C-rates of the dd-MnZr/CNF sample are shown in Figure 12e. The initial charge and discharge capacities were 41.9 and 40.0mAh/g, respectively, similar to the value of the h-10%MnZr/CNF cathode. In this case, the capacity was rather stable at low C-rates, and the capacity loss became remarkable only at C-rates higher than 0.2C. Indeed, the average capacity values were 46.7, 44.5, and 43.6 mAh/g at 0.05C, 0.1C, and 0.2C, 31.6 and 17.0 mAh/g at 0.5C and 1C, and 12.0, 8.7, 6.5, and 4.5 mAh/g at 2C, 5C, 10C, and 20C, respectively. The capacity was completely recovered at the end of the measurement, and a Coulombic efficiency $\geq 94\%$ was reached.

Hence, the dd-MnZr/CNF self-standing cathode displayed better electrochemical performances than the h-MnZr/CNF electrodes but worse than the v-30%MnZr/CNF one. These results can be explained by the higher amount of active material (33 wt%) present in the CNFs compared to that in the horizontal samples (9.3 and 21.8 wt%). However, the active materials aggregates were non-homogeneously distributed along the CNF sheets' thickness and were preferentially located on their surface, and this undoubtedly affected the electrochemical performance. The charge/discharge investigation suggested a superior performance of all the self-standing cathodes in terms of a specific capacity at high C-rates and Coulombic efficiency compared to the tape-cast counterpart. The Coulombic efficiency values of all the MnZr/CNFs electrodes approached the CE% reported in the literature for other binder-free electrodes tested for cycles at different C-rates, typically ranging between 95% and 99% [55,65,66]. Notably, the v-30%MnZr/CNF cathode exhibited both high loading (29.8 wt%) and homogeneous distribution of the active material, and improved electrochemical performances were expected.

Figure 12f compares the average discharge capacities of all the investigated cathodes at the different C-rates. All the MnZr/CNF self-standing electrodes exhibited improved electrochemical performances compared to the p-MnZr slurry cathode. Indeed, independently of the $\text{Na}_3\text{MnZr}(\text{PO}_4)_3$ amount in the CNF sheets, the self-standing electrodes were performant at C-rates higher than 5C, and the higher the active material amount, the higher the capacity value at each C-rate. These results confirmed the beneficial role of CNFs, especially at high C-rates, when the required fast ion diffusion is invalidated in packed materials such as tape-cast cathodes [57,58]. However, among the three approaches applied to synthesize the self-standing electrodes, the dip-drop method gave intermediate values between the horizontal and vertical settings in terms of both the capacity value and the electrochemical performance at a high C-rate. The best electrochemical results were obtained for the v-30%MnZr/CNF cathode, which exhibited not only the highest initial capacity values but also the best performance at high C-rates. The reported results confirmed that the vertical set-up provided the best self-standing electrode. Based on this, we completed our investigation by testing the long cycling capability and lifespan of the v-30%MnZr/CNF sample compared to the slurry one. We wanted to confirm that the right synthesis of a self-standing electrode gives a cathode with longer cycling and better performances at high C-rates than the slurry one, thanks to CNFs' properties.

The long charge/discharge cycling of the two cathodes is shown in Figure 13.

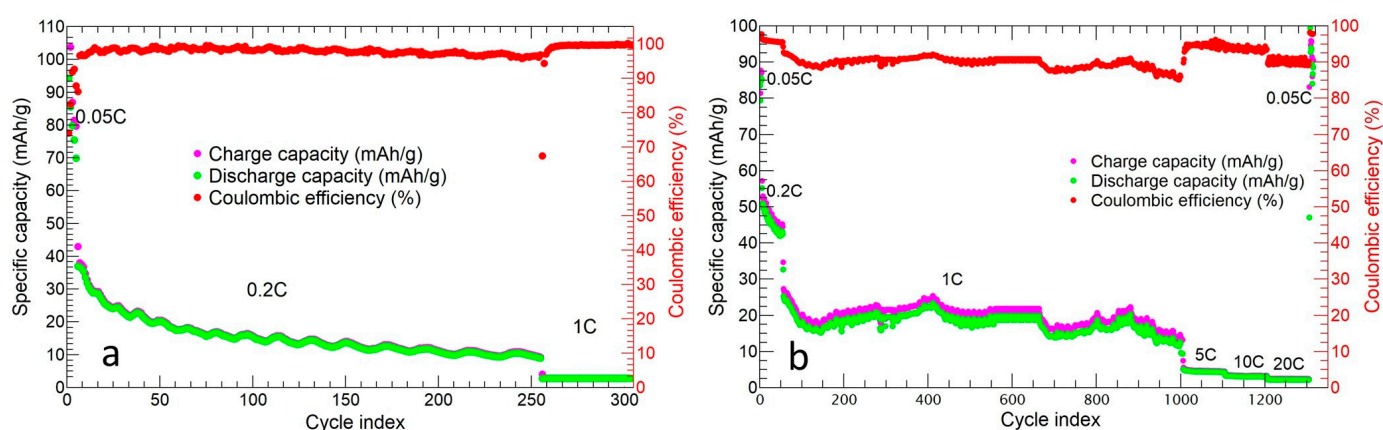


Figure 13. Cycling performance of (a) p-MnZr slurry electrode and (b) v-30%MnZr/CNF self-standing cathode.

The tape-cast cathode (Figure 13a) was tested at 0.05C, 0.2C, and 1C for 5, 200, and 100 cycles. After the initial charge and discharge specific capacity of 104.3 mAh/g and 94.2 mAh/g, respectively, the cell underwent a specific capacity loss: a value of 16.5 mAh/g was achieved during the 82nd cycle at 0.2C. This specific capacity value was quite constant

up until the 200th cycle at 0.2C, with a capacity retention of 15.8% and an average Coulombic efficiency $\geq 98\%$. When the cell was tested at 1C, the specific capacity decreased down to 2.6 mAh/g and could not be further cycled at 0.05C.

The v-30%MnZr/CNF self-standing cathode was tested at 0.05C, 0.2C, 1C, 5C, 10C, and 20C for 5, 50, 1000, 100, 50, and 30 cycles, respectively (Figure 13b). The initial charge and discharge capacities at 0.05C were 87.2 mAh/g and 85.4 mAh/g, respectively. Then, a discharge capacity loss was detected (45.2 mAh/g at 0.2C for 50 cycles), as well as average values of the discharge capacity of 19.3 mAh/g at 1C, 4.2 mAh/g at 5C, 3.7 mAh/g at 10C, and 2.5 mAh/g at 20C. The average Coulombic efficiency was $\geq 91\%$, approaching those obtained for other electrode materials, such as NaVPO₄F/CNF after 50 cycles [53]. The capacity was completely recovered at the end of the measurement in the last cycle at 0.05C, and the capacity retention at 0.2C for 50 cycles and at 1C for 1000 cycles was 52.9% and 22.6%, respectively. We can conclude that, contrary to the p-MnZr slurry cathode, the v-30%MnZr/CNF self-standing electrode presented a better capacity value at each C-rate, and it worked at a high C-rate after 1000 cycles at 1C too. Moreover, it also showed better capacity retention at both 0.2C and 1C.

An electrochemical impedance spectroscopy (EIS) analysis was performed on the v-30%MnZr/CNF and p-MnZr cathodes to further investigate the effect of CNFs on the kinetic process of the self-standing electrodes. The Nyquist plot and the equivalent circuit are shown in Figure S4 (Supplementary Materials). The EIS spectra were consistent with those reported in the literature for the Na₃MnZr(PO₄)₃ active material [41]. The smaller diameter of the semicircle in the high-frequency region for the v-30%MnZr/CNF electrode suggested a smaller charge transfer resistance (807 Ω vs. 1092 Ω of the tape-cast cathode) and a faster charge transfer at the electrode–electrolyte interface. Moreover, the decrease in electrolyte resistance in the self-standing electrode (10.7 Ω vs. 24.2 Ω for the tape-cast counterpart) suggested a better electrolyte permeation into MnZr/CNF electrodes, thanks to the presence of a CNF porous matrix. Finally, the larger slope of Warburg impedance for v-30%MnZr/CNF than for the p-MnZr cathode indicated that the more favorable Na ion transport was in the self-standing electrode.

The reported results put into evidence the advantages of using CNFs to assemble cathodes for SIBs. An improved electrochemical performance was obtained, as they enhanced the electronic conductivity and guaranteed good electrolyte–active material contact, thanks to the easy permeation of the electrolyte into their CNF porous matrix. Notably, the CNFs demonstrated to be a suitable support to realize free-standing electrodes, allowing us to avoid the use of Al foils as the current collectors. Among the synthetic approaches to prepare electrospun active material–carbon nanofibers cathodes (see Figure 1), better electrochemical performances in terms of capacity values and lifespan were obtained for a higher Na₃MnZr(PO₄)₃ amount, reached by using a vertical setting in the electrospinning process: in this case, the active material particles, pre-synthesized via sol–gel, were quantitatively deposited in the CNF sheets, compared to the horizontal setting. When a comparable active material amount was loaded into CNFs (v-30%MnZr/CNF and dd-MnZr/CNF samples), the best performances were obtained by dispersing the pre-synthesized Na₃MnZr(PO₄)₃ powder into the polymeric solution to be electrospun, as this approach allowed a homogeneous dispersion of the active material along the CNF sheets, and the agglomerates were present both within and embedded into the CNFs. On the contrary, in the dip–drop approach, the active material was preferentially distributed on the sheets' surface and on the external surface of the carbon nanotubes.

3. Materials and Methods

3.1. Materials

The chemicals (Sigma-Aldrich, Milano, Italy) were of a reagent-grade or higher quality. Citric acid (C₆H₈O₇), ammonium phosphate monobasic (NH₄H₂PO₄), sodium acetate (CH₃COONa) manganese(II) acetate tetrahydrate ((CH₃COO)₂Mn · 4H₂O), zirconium(IV) acetylacetonate (Zr(C₅H₇O₂)₄), 1M sodium perchlorate in PC (1:1 v:v) electrolyte,

fluoroethylene carbonate (FEC), carbon acetylene black powder, poly(vinylidene fluoride) (PVdF), polyacrylonitrile (PAN: $(C_3H_3N)_n$), and *N,N*-dimethylacetamide (DMAc: $CH_3CON(CH_3)_2$) were employed.

3.2. Synthesis

3.2.1. Active Material $Na_3MnZr(PO_4)_3$

The $Na_3MnZr(PO_4)_3$ synthesis procedure reported in [38] was followed. Based on $Na_3MnZr(PO_4)_3$ stoichiometry, an aqueous solution of CH_3OONa , $(CH_3COO)_2Mn \cdot 4H_2O$, $NH_4H_2PO_4$, and $Zr(C_5H_7O_2)_4$ was prepared. To the solution was added citric acid (citric acid moles equals the total transition metal ones) as the chelating agent, in order to obtain the carbon coating of the active material aggregates. The solution was heated at 80 °C to obtain the gel that was dried at 100 °C in an oven. The product was ground in an agate mortar and treated at 750 °C for 10h under a nitrogen flux in a tube furnace (Carbolite). The final powder product (pristine product) was called p-MnZr.

3.2.2. Self-Standing Cathodes

As reported in Section 2 and Figure 1, two different approaches were proposed to prepare the self-standing electrodes, differing in the method employed to load the active material onto CNFs and the electrospinning setting. For the horizontal depositions, a EF050-Starter Kit Electrospinning of SKE Research Equipment (C/O Leonardo S.r.l, Bollate, MI, Italy) was used. A home-made humidity control box was used to achieve humidity values lower than 20%. An electrospinning apparatus, NANON01A, equipped with a dehumidifier (MEEC instruments, MP, Pioltello, Italy) was employed to produce vertical depositions.

In the dip-drop procedure, the pure carbon nanofibers (CNF sample) were prepared first: 8 wt% PAN solution in DMAc was electrospun (horizontal setting) with 3.5 mL/h rate, 16 gauge needle, applied voltage 14 kV, and a needle-collector distance of 18cm. Once the collected CNF sheets were removed from the support (aluminum foil), the CNFs were thermally treated: for the stabilization process, the CNFs were heated for 30 min at 100 °C, for 30 min at 200 °C, and, finally, for 2 h at 260 °C (heating ramp: 5 °C min⁻¹) in air, while the carbonization process was conducted in a tubular furnace (Carbolite) at 900 °C for 2 h (heating ramp: 10 °C min⁻¹) under a nitrogen atmosphere. For the dip-drop process, a solution containing the active material precursors and citric acid was prepared following the reagent quantities used in sol-gel synthesis (see Section 3.2.1). The carbonized CNF sheet was deeply drenched in the solution of active material reagents, then the same solution was dropped on the CNF sheet surface. The $Na_3MnZr(PO_4)_3$ precursor-soaked-CNF sheet was dried under a vacuum at 120 °C for one night and thermal-treated like the sol-gel sample: 750 °C for 10 h under a nitrogen atmosphere. The obtained self-standing cathode was called dd-MnZr/CNF.

In the second synthetic approach, the $Na_3MnZr(PO_4)_3$ powder (p-MnZr sample) was ball-milled at 100 rpm for two cycles (20 min each), then 10 wt% (0.188g) or 30 wt% (0.564g) of p-MnZr was added to 25 mL of *N,N*-dimethylacetamide, and the suspension was sonicated 1 h. Then, 1.88 g PAN was added, and the suspension was stirred overnight at 60 °C. The obtained dispersions were electrospun using a horizontal setting apparatus (samples called h-10%MnZr/CNF and h-30%MnZr/CNF). The 30 wt% dispersion was also electrospun employing a vertical equipment (sample named v-30%MnZr/CNF). Using horizontal deposition electrospinning, the setting parameters were optimized as follows: 10.5 mL dispersion, 3.5 mL/h flow, 16 gauge needle, applied voltage 18 kV, needle-collector distance 18 cm, deposition time 3 h, temperature and relative humidity values equal to 25 °C and lower than 20%, respectively, during each deposition. Instead, for vertical deposition electrospinning, the parameters were set as follows: 10 mL dispersion, 0.5 mL/h flow rate, 16 gauge needle, applied voltage 28 kV, needle-collector distance 15 cm, deposition time 3h, and temperature and relative humidity values equal to 23 ± 2 °C and 20 ± 3%, respectively, during each deposition.

Both horizontally and vertically deposited self-standing electrodes were removed from the support and underwent stabilization (30 min at 100 °C, 30 min at 200 °C, and 2 h at 260 °C in air) and the carbonization process at 750 °C in N₂ flux.

3.2.3. Tape-Cast Cathode

The p-MnZr active material was first ball-milled at 100 rpm for two cycles (20 min each). The slurry was obtained by dispersing 70 wt% active material, 20 wt% acetylene carbon, and 10 wt% PVdF binder (Solvay 5130) in distilled water. The slurry was magnetically stirred for 2 h, and then it was tape-cast (Doctor Blade coating technique) on aluminum foils and dried at 70 °C for 3 h.

3.3. Cell Assembly

Swagelok-type cells were assembled in an argon-filled dry box (MBraun; H₂O content < 0.1 ppm, O₂ content < 0.1 ppm). NaClO₄ 1M in PC and 5 wt% FEC was used as the electrolyte, and sodium foil was used as the counter-electrode. The working and counter-electrode showed a diameter of 1 cm.

3.4. Characterization Techniques

For the X-ray powder diffraction (XRPD) analysis, a Bruker D5005 diffractometer (Bruker, Karlsruhe, Germany) equipped with a Cu K α radiation tube (40 kV, 40 mA), a curved graphite monochromator on the diffracted beam, and a scintillation detector was used. The patterns collection conditions were the following: 16–80° 2-theta range, 0.03° step size, and 22 s/step counting time. The TOPAS 3.0 software [67] was used for the Rietveld structural refinement of the p-MnZr and MnZr/CNFs samples.

Room temperature micro-Raman measurements were performed using an integrated confocal micro-Raman spectrometer, XploRA Plus HORIBA Scientific, equipped with an Olympus microscope BX43. Green laser light at 532 nm was used for excitation tuning the 100 mW output power through a set of neutral filters with different optical densities. The samples were positioned on a motorized xy stage automatically controlled, allowing mapping acquisitions. The spectral resolution was about 3 cm⁻¹. The measurements were performed using a long work distance 50 \times magnification objective with a spatial resolution of the order of 4 microns. The spectra were acquired with a mean integration time of about 10 s and a number of accumulations equal to 10. All the reported data were obtained as an average spectrum, sampling the materials in several different regions.

The scanning electron microscopy images were taken with a Zeiss EVO MA10 (Carl Zeiss, Oberkochen, Germany) microscope, equipped with an energy dispersive detector for EDS analysis, on gold-sputtered samples (20 kV, secondary electrons images, working distance of 8.5 mm).

The transmission electron microscopy images were collected with a JEOL JEM-1200EXIII equipped with a TEM CCD camera Mega View III transmission electron microscope. The samples were dispersed in water; a drop of about 0.7 μ L was deposited on the formvar/carbon-coated Ni grid and dried.

For the thermogravimetric analysis, a TGA Q5000 IR apparatus interfaced with a TA 5000 data station (TA Instruments, Newcastle, DE, USA) was employed. The thermogravimetric data were collected in the 25–750 °C temperature range in air (heating rate: 10 °C min⁻¹).

The electrochemical properties of the tape-cast and self-standing cathodes were investigated at room temperature on a Swagelok cell. For cyclic voltammetry (CV), an Autolab PGSTAT30 potentiostat (Eco Chemie) in the 2.5–4.5 V potential range was used, and the data were processed with the GPES V4.9 software. For the galvanostatic charge/discharge cycles, we used a Neware-4000BTS battery testing system at different current rates in the 2.5–4.5 V potential range. The electrochemical impedance spectroscopy (EIS) measurements were performed on an Autolab PGSTAT30 potentiostat (Eco Chemie). The EIS spectra were acquired at OCV in the 10⁶–10⁻² Hz frequency range with an amplitude potential of 1 mV.

4. Conclusions

In this study, different synthetic approaches based on the electrospinning technique were applied to prepare $\text{Na}_3\text{MnZr}(\text{PO}_4)_3/\text{CNF}$ free-standing cathodes for SIBs. Independently of the method employed, the active material was successfully loaded into CNFs and its NASICON-type crystal structure was maintained. Indeed, the synthesis route had an impact on the loaded active material amount and distribution through the carbon nanofiber sheets. Compared to the dip-drop coating, the dispersion of the pre-synthesized active material method allowed the homogeneous distribution of the $\text{Na}_3\text{MnZr}(\text{PO}_4)_3$ particles along the thickness of the sheet, and the aggregates connected and covered the surface of the CNFs but were also embedded into them: this active material–CNF intimate contact resulted beneficial to the electrochemical performances. Concerning the setting, the vertical one seemed more efficient, as particulate decantation was avoided, and the active material was quantitatively loaded into the CNFs. Indeed, the v-30%MnZr/CNF sample displayed the best electrochemical performances.

Independently of the synthetic approach, an improved electrochemical performance in terms of specific discharge capacities at different C-rates was achieved in the self-standing cathodes compared to the tape-cast one. Notably, the enhancement was particularly evident at high C-rates, where the porous nature of the non-woven nanofibers guaranteed electrolyte diffusion and easy contact with the active material aggregates. The best electrochemical performances were achieved by the v-30%MnZr/CNF electrode, which also demonstrated a promising long cycling life compared to the tape-cast counterpart. The reported results suggest that the ex situ synthesis of $\text{Na}_3\text{MnZr}(\text{PO}_4)_3$ and its addition (30 wt%) to the carbon precursor solution to be electrospun with a vertical setting are a simple and feasible approach to obtaining self-standing cathodes with enhanced electrochemical performances compared to tape-casted cathodes (70 wt% of active material).

Supplementary Materials: The following supporting information can be downloaded at <https://www.mdpi.com/article/10.3390/molecules29081885/s1>: Figure S1: Rietveld refinement of the X-ray diffraction data of the p-MnZr sample; Figure S2: Rietveld refinement of the X-ray diffraction data of the MnZr/CNF samples; Figure S3: CV and charge/discharge profiles of the tape-cast and self-standing MnZr/CNF cathodes; Figure S4: Nyquist plot of the v-30%MnZr/CNF and p-MnZr cathodes; Table S1: Lattice parameters, cell volume, c/a ratio, crystallite size, and discrepancy factors obtained by the Rietveld refinement of the diffraction data of the pristine and CNF-loaded $\text{Na}_3\text{MnZr}(\text{PO}_4)_3$ samples.

Author Contributions: Conceptualization, D.C. and D.M.C.; formal analysis, D.C., D.M.C. and P.G.; investigation, D.M.C., C.U., B.A., V.B., S.P. and G.B.; resources, D.C.; writing—original draft preparation, D.C., D.M.C. and P.G.; writing—review and editing, D.C., D.M.C., P.G., C.M. and C.U.; visualization, D.M.C., C.U. and B.A. All authors have read and agreed to the published version of the manuscript.

Funding: This research received no external funding.

Institutional Review Board Statement: Not applicable.

Informed Consent Statement: Not applicable.

Data Availability Statement: The data presented in this study are available upon request from the corresponding author.

Acknowledgments: The authors are grateful to Massimo Boiocchi for the support in the TEM analysis performed at the Centro Grandi Strumenti, University of Pavia, and to Matteo Lugli from the Department of Physics at the University of Pavia for the fabrication of a handmade humidity control system for the electrospinning process. The authors acknowledge support from the Ministero dell'Università e della Ricerca (MUR) and the University of Pavia through the program "Dipartimenti di Eccellenza 2023–2027".

Conflicts of Interest: The authors declare no conflicts of interest.

References

1. Goodenough, J.B. Electrochemical Energy Storage in a Sustainable Modern Society. *Energy Environ. Sci.* **2013**, *7*, 14–18. [[CrossRef](#)]
2. Larcher, D.; Tarascon, J.-M. Towards Greener and More Sustainable Batteries for Electrical Energy Storage. *Nat. Chem.* **2015**, *7*, 19–29. [[CrossRef](#)] [[PubMed](#)]
3. Scrosati, B.; Hassoun, J.; Sun, Y.-K. Lithium-Ion Batteries. A Look into the Future. *Energy Environ. Sci.* **2011**, *4*, 3287–3295. [[CrossRef](#)]
4. Gao, C.; Dong, Q.; Zhang, G.; Fan, H.; Li, H.; Hong, B.; Lai, Y. Antimony-Doped Lithium Phosphate Artificial Solid Electrolyte Interphase for Dendrite-Free Lithium-Metal Batteries. *ChemElectroChem* **2019**, *6*, 1134–1138. [[CrossRef](#)]
5. Huang, Y.; Yang, H.; Xiong, T.; Adekoya, D.; Qiu, W.; Wang, Z.; Zhang, S.; Balogun, M.-S. Adsorption Energy Engineering of Nickel Oxide Hybrid Nanosheets for High Areal Capacity Flexible Lithium-Ion Batteries. *Energy Storage Mater.* **2020**, *25*, 41–51. [[CrossRef](#)]
6. Balogun, M.-S.; Zeng, Y.; Qiu, W.; Luo, Y.; Onasanya, A.; Olaniyi, T.K.; Tong, Y. Three-Dimensional Nickel Nitride (Ni₃N) Nanosheets: Free Standing and Flexible Electrodes for Lithium Ion Batteries and Supercapacitors. *J. Mater. Chem. A* **2016**, *4*, 9844–9849. [[CrossRef](#)]
7. Balogun, M.-S.; Wu, Z.; Luo, Y.; Qiu, W.; Fan, X.; Long, B.; Huang, M.; Liu, P.; Tong, Y. High Power Density Nitridated Hematite (α -Fe₂O₃) Nanorods as Anode for High-Performance Flexible Lithium Ion Batteries. *J. Power Sources* **2016**, *308*, 7–17. [[CrossRef](#)]
8. Tarascon, J.-M. Is Lithium the New Gold? *Nature Chem.* **2010**, *2*, 510. [[CrossRef](#)] [[PubMed](#)]
9. Whittingham, M.S. Lithium Batteries and Cathode Materials. *Chem. Rev.* **2004**, *104*, 4271–4302. [[CrossRef](#)] [[PubMed](#)]
10. Goodenough, J.B.; Park, K.-S. The Li-Ion Rechargeable Battery: A Perspective. *J. Am. Chem. Soc.* **2013**, *135*, 1167–1176. [[CrossRef](#)] [[PubMed](#)]
11. Grosjean, C.; Miranda, P.H.; Perrin, M.; Poggi, P. Assessment of World Lithium Resources and Consequences of Their Geographic Distribution on the Expected Development of the Electric Vehicle Industry. *Renew. Sustain. Energy Rev.* **2012**, *16*, 1735–1744. [[CrossRef](#)]
12. Kesler, S.E.; Gruber, P.W.; Medina, P.A.; Keoleian, G.A.; Everson, M.P.; Wallington, T.J. Global Lithium Resources: Relative Importance of Pegmatite, Brine and Other Deposits. *Ore Geol. Rev.* **2012**, *48*, 55–69. [[CrossRef](#)]
13. Miedema, J.H.; Moll, H.C. Lithium Availability in the EU27 for Battery-Driven Vehicles: The Impact of Recycling and Substitution on the Confrontation between Supply and Demand Until 2050. *Resour. Policy* **2013**, *38*, 204–211. [[CrossRef](#)]
14. Vaalma, C.; Buchholz, D.; Weil, M.; Passerini, S. A Cost and Resource Analysis of Sodium-Ion Batteries. *Nat. Rev. Mater.* **2018**, *3*, 18013. [[CrossRef](#)]
15. Zhao, C.; Wang, Q.; Yao, Z.; Wang, J.; Sánchez-Lengeling, B.; Ding, F.; Qi, X.; Lu, Y.; Bai, X.; Li, B.; et al. Rational Design of Layered Oxide Materials for Sodium-Ion Batteries. *Science* **2020**, *370*, 708–711. [[CrossRef](#)] [[PubMed](#)]
16. Liu, Y.; Liu, X.; Wang, T.; Fan, L.-Z.; Jiao, L. Research and Application Progress on Key Materials for Sodium-Ion Batteries. *Sustain. Energy Fuels* **2017**, *1*, 986–1006. [[CrossRef](#)]
17. Han, M.H.; Gonzalo, E.; Singh, G.; Rojo, T. A Comprehensive Review of Sodium Layered Oxides: Powerful Cathodes for Na-Ion Batteries. *Energy Environ. Sci.* **2014**, *8*, 81–102. [[CrossRef](#)]
18. Wang, P.-F.; You, Y.; Yin, Y.-X.; Guo, Y.-G. Layered Oxide Cathodes for Sodium-Ion Batteries: Phase Transition, Air Stability, and Performance. *Adv. Energy Mater.* **2018**, *8*, 1701912. [[CrossRef](#)]
19. Zhou, Y.-N.; Wang, P.-F.; Niu, Y.-B.; Li, Q.; Yu, X.; Yin, Y.-X.; Xu, S.; Guo, Y.-G. A P2/P3 Composite Layered Cathode for High-Performance Na-Ion Full Batteries. *Nano Energy* **2019**, *55*, 143–150. [[CrossRef](#)]
20. Xie, Y.; Wang, H.; Xu, G.; Wang, J.; Sheng, H.; Chen, Z.; Ren, Y.; Sun, C.-J.; Wen, J.; Wang, J.; et al. In Operando XRD and TXM Study on the Metastable Structure Change of NaNi_{1/3}Fe_{1/3}Mn_{1/3}O₂ under Electrochemical Sodium-Ion Intercalation. *Adv. Energy Mater.* **2016**, *6*, 1601306. [[CrossRef](#)]
21. Wei, F.; Zhang, Q.; Zhang, P.; Tian, W.; Dai, K.; Zhang, L.; Mao, J.; Shao, G. Review—Research Progress on Layered Transition Metal Oxide Cathode Materials for Sodium Ion Batteries. *J. Electrochem. Soc.* **2021**, *168*, 050524. [[CrossRef](#)]
22. Wang, H.; Zhou, L.; Cheng, Z.; Liu, L.; Wang, Y.; Du, T. Recent Advances on F-Doped Layered Transition Metal Oxides for Sodium Ion Batteries. *Molecules* **2023**, *28*, 8065. [[CrossRef](#)] [[PubMed](#)]
23. Wang, L.; Lu, Y.; Liu, J.; Xu, M.; Cheng, J.; Zhang, D.; Goodenough, J.B. A Superior Low-Cost Cathode for a Na-Ion Battery. *Angew. Chem. Int. Ed.* **2013**, *52*, 1964–1967. [[CrossRef](#)] [[PubMed](#)]
24. Lee, H.-W.; Wang, R.Y.; Pasta, M.; Woo Lee, S.; Liu, N.; Cui, Y. Manganese Hexacyanomanganate Open Framework as a High-Capacity Positive Electrode Material for Sodium-Ion Batteries. *Nat. Commun.* **2014**, *5*, 5280. [[CrossRef](#)] [[PubMed](#)]
25. You, Y.; Wu, X.-L.; Yin, Y.-X.; Guo, Y.-G. High-Quality Prussian Blue Crystals as Superior Cathode Materials for Room-Temperature Sodium-Ion Batteries. *Energy Environ. Sci.* **2014**, *7*, 1643–1647. [[CrossRef](#)]
26. Song, J.; Wang, L.; Lu, Y.; Liu, J.; Guo, B.; Xiao, P.; Lee, J.-J.; Yang, X.-Q.; Henkelman, G.; Goodenough, J.B. Removal of Interstitial H₂O in Hexacyanometalates for a Superior Cathode of a Sodium-Ion Battery. *J. Am. Chem. Soc.* **2015**, *137*, 2658–2664. [[CrossRef](#)] [[PubMed](#)]
27. Ren, W.; Qin, M.; Zhu, Z.; Yan, M.; Li, Q.; Zhang, L.; Liu, D.; Mai, L. Activation of Sodium Storage Sites in Prussian Blue Analogues via Surface Etching. *Nano Lett.* **2017**, *17*, 4713–4718. [[CrossRef](#)] [[PubMed](#)]
28. Ma, X.; Pan, Z.; Wu, X.; Shen, P.K. Na₄Fe₃(PO₄)₂(P₂O₇)@NaFePO₄@C Core-Double-Shell Architectures on Carbon Cloth: A High-Rate, Ultrastable, and Flexible Cathode for Sodium Ion Batteries. *Chem. Eng. J.* **2019**, *365*, 132–141. [[CrossRef](#)]

29. Zhang, J.; Zhao, X.; Song, Y.; Li, Q.; Liu, Y.; Chen, J.; Xing, X. Understanding the Superior Sodium-Ion Storage in a Novel $\text{Na}_{3.5}\text{Mn}_{0.5}\text{V}_{1.5}(\text{PO}_4)_3$ Cathode. *Energy Storage Mater.* **2019**, *23*, 25–34. [[CrossRef](#)]
30. Liu, R.; Liang, Z.; Xiang, Y.; Zhao, W.; Liu, H.; Chen, Y.; An, K.; Yang, Y. Recognition of $\text{V}^{3+}/\text{V}^{4+}/\text{V}^{5+}$ Multielectron Reactions in $\text{Na}_3\text{V}(\text{PO}_4)_2$: A Potential High Energy Density Cathode for Sodium-Ion Batteries. *Molecules* **2020**, *25*, 1000. [[CrossRef](#)] [[PubMed](#)]
31. Wang, C.; Du, D.; Song, M.; Wang, Y.; Li, F. A High-Power $\text{Na}_3\text{V}_2(\text{PO}_4)_3$ -Bi Sodium-Ion Full Battery in a Wide Temperature Range. *Adv. Energy Mater.* **2019**, *9*, 1900022. [[CrossRef](#)]
32. Xu, Y.; Wei, Q.; Xu, C.; Li, Q.; An, Q.; Zhang, P.; Sheng, J.; Zhou, L.; Mai, L. Layer-by-Layer $\text{Na}_3\text{V}_2(\text{PO}_4)_3$ Embedded in Reduced Graphene Oxide as Superior Rate and Ultralong-Life Sodium-Ion Battery Cathode. *Adv. Energy Mater.* **2016**, *6*, 1600389. [[CrossRef](#)]
33. Li, F.; Zhu, Y.-E.; Sheng, J.; Yang, L.; Zhang, Y.; Zhou, Z. GO-Induced Preparation of Flake-Shaped $\text{Na}_3\text{V}_2(\text{PO}_4)_3$ @rGO as High-Rate and Long-Life Cathodes for Sodium-Ion Batteries. *J. Mater. Chem. A* **2017**, *5*, 25276–25281. [[CrossRef](#)]
34. Kawai, K.; Zhao, W.; Nishimura, S.; Yamada, A. High-Voltage $\text{Cr}^{4+}/\text{Cr}^{3+}$ Redox Couple in Polyanion Compounds. *ACS Appl. Energy Mater.* **2018**, *1*, 928–931. [[CrossRef](#)]
35. Rajagopalan, R.; Chen, B.; Zhang, Z.; Wu, X.-L.; Du, Y.; Huang, Y.; Li, B.; Zong, Y.; Wang, J.; Nam, G.-H.; et al. Improved Reversibility of $\text{Fe}^{3+}/\text{Fe}^{4+}$ Redox Couple in Sodium Super Ion Conductor Type $\text{Na}_3\text{Fe}_2(\text{PO}_4)_3$ for Sodium-Ion Batteries. *Adv. Mater.* **2017**, *29*, 1605694. [[CrossRef](#)] [[PubMed](#)]
36. Chen, K.; Shi, Q.; Wang, Y.; Li, X.; Jiang, Y.; Xu, H.; Guo, S.; Zhao, L.; Dai, C. Effects of Scandium Doping on the Electrochemical Performance of Cathode Materials $\text{Na}_3\text{MnTi}(\text{PO}_4)_3$ for Sodium-Ion Batteries. *Colloids Surf. A Physicochem. Eng. Asp.* **2023**, *662*, 130996. [[CrossRef](#)]
37. Li, H.; Xu, M.; Gao, C.; Zhang, W.; Zhang, Z.; Lai, Y.; Jiao, L. Highly Efficient, Fast and Reversible Multi-Electron Reaction of $\text{Na}_3\text{MnTi}(\text{PO}_4)_3$ Cathode for Sodium-Ion Batteries. *Energy Storage Mater.* **2020**, *26*, 325–333. [[CrossRef](#)]
38. Gao, H.; Seymour, I.D.; Xin, S.; Xue, L.; Henkelman, G.; Goodenough, J.B. $\text{Na}_3\text{MnZr}(\text{PO}_4)_3$: A High-Voltage Cathode for Sodium Batteries. *J. Am. Chem. Soc.* **2018**, *140*, 18192–18199. [[CrossRef](#)] [[PubMed](#)]
39. Liu, J.; Zhao, Y.; Huang, X.; Zhou, Y.; Lam, K.; Yu, D.Y.W.; Hou, X. NASICON-Structured $\text{Na}_3\text{MnTi}(\text{PO}_4)_{2.83}\text{F}_{0.5}$ Cathode with High Energy Density and Rate Performance for Sodium-Ion Batteries. *Chem. Eng. J.* **2022**, *435*, 134839. [[CrossRef](#)]
40. Zhu, T.; Hu, P.; Cai, C.; Liu, Z.; Hu, G.; Kuang, Q.; Mai, L.; Zhou, L. Dual Carbon Decorated $\text{Na}_3\text{MnTi}(\text{PO}_4)_3$: A High-Energy-Density Cathode Material for Sodium-Ion Batteries. *Nano Energy* **2020**, *70*, 104548. [[CrossRef](#)]
41. Ma, X.; Wu, X.; Liu, Y.; Wu, W.; Pan, Z.; Shen, P.K. Toward a High-Energy-Density Cathode with Enhanced Temperature Adaptability for Sodium-Ion Batteries: A Case Study of $\text{Na}_3\text{MnZr}(\text{PO}_4)_3$ Microspheres with Embedded Dual-Carbon Networks. *ACS Appl. Mater. Interfaces* **2021**, *13*, 21390–21400. [[CrossRef](#)] [[PubMed](#)]
42. Sun, G.; Sun, L.; Xie, H.; Liu, J. Electrospinning of Nanofibers for Energy Applications. *Nanomaterials* **2016**, *6*, 129. [[CrossRef](#)] [[PubMed](#)]
43. Liao, Q.; Kim, E.J.; Tang, Y.; Xu, H.; Yu, D.-G.; Song, W.; Kim, B.J. Rational Design of Hyper-Crosslinked Polymers for Biomedical Applications. *J. Polym. Sci.* **2023**, *64*, 8. [[CrossRef](#)]
44. Song, W.; Zhang, M.; Huang, X.; Chen, B.; Ding, Y.; Zhang, Y.; Yu, D.G.; Kim, I. Smart l-Borneol-Loaded Hierarchical Hollow Polymer Nanospheres with Antipollution and Antibacterial Capabilities. *Mater. Today Chem.* **2022**, *26*, 101252. [[CrossRef](#)]
45. Peña, A.; Guerrero, A.; Puerta, J.; Brito, J.L.; Heckel, T.K. Characterisation of Carbon Nanotube Foam for Improved Gas Storage Capability. In Proceedings of the Experimental Mechanics on Emerging Energy Systems and Materials; Proulx, T., Ed.; Springer: New York, NY, USA, 2011; Volume 5, pp. 11–16.
46. Kretzschmar, A.; Selmert, V.; Weinrich, H.; Kungl, H.; Tempel, H.; Eichel, R.-A. Tailored Gas Adsorption Properties of Electrospun Carbon Nanofibers for Gas Separation and Storage. *ChemSusChem* **2020**, *13*, 3180–3191. [[CrossRef](#)] [[PubMed](#)]
47. Díaz, E.; León, M.; Ordóñez, S. Hydrogen Adsorption on Pd-Modified Carbon Nanofibres: Influence of CNF Surface Chemistry and Impregnation Procedure. *Int. J. Hydrogen Energy* **2010**, *35*, 4576–4581. [[CrossRef](#)]
48. Takahashi, Y.; Fujita, H.; Sakoda, A. Adsorption of Ammonia and Water on Functionalized Edge-Rich Carbon Nanofibers. *Adsorption* **2013**, *19*, 143–159. [[CrossRef](#)]
49. Verma, S.; Sinha-Ray, S.; Sinha-Ray, S. Electrospun CNF Supported Ceramics as Electrochemical Catalysts for Water Splitting and Fuel Cell: A Review. *Polymers* **2020**, *12*, 238. [[CrossRef](#)] [[PubMed](#)]
50. Zhang, B.; Yu, Y.; Xu, Z.-L.; Abouali, S.; Akbari, M.; He, Y.-B.; Kang, F.; Kim, J.-K. Correlation Between Atomic Structure and Electrochemical Performance of Anodes Made from Electrospun Carbon Nanofiber Films. *Adv. Energy Mater.* **2014**, *4*, 1301448. [[CrossRef](#)]
51. Li, H.; Bai, Y.; Wu, F.; Li, Y.; Wu, C. Budding Willow Branches Shaped $\text{Na}_3\text{V}_2(\text{PO}_4)_3/\text{C}$ Nanofibers Synthesized via an Electrospinning Technique and Used as Cathode Material for Sodium Ion Batteries. *J. Power Sources* **2015**, *273*, 784–792. [[CrossRef](#)]
52. Liu, Y.; Wang, F.; Fan, L.-Z. Self-Standing Na-Storage Anode of Fe_2O_3 Nanodots Encapsulated in Porous N-Doped Carbon Nanofibers with Ultra-High Cyclic Stability. *Nano Res.* **2018**, *11*, 4026–4037. [[CrossRef](#)]
53. Jin, T.; Liu, Y.; Li, Y.; Cao, K.; Wang, X.; Jiao, L. Electrospun $\text{NaVPO}_4\text{F}/\text{C}$ Nanofibers as Self-Standing Cathode Material for Ultralong Cycle Life Na-Ion Batteries. *Adv. Energy Mater.* **2017**, *7*, 1700087. [[CrossRef](#)]
54. Conti, D.M.; Fusaro, C.; Bruni, G.; Galinetto, P.; Albini, B.; Milanese, C.; Berbenni, V.; Capsoni, D. ZnS-rGO/CNF Free-Standing Anodes for SIBs: Improved Electrochemical Performance at High C-Rate. *Nanomaterials* **2023**, *13*, 1160. [[CrossRef](#)] [[PubMed](#)]
55. Yu, S.; Liu, Z.; Tempel, H.; Kungl, H.; Eichel, R.-A. Self-Standing NASICON-Type Electrodes with High Mass Loading for Fast-Cycling All-Phosphate Sodium-Ion Batteries. *J. Mater. Chem. A* **2018**, *6*, 18304–18317. [[CrossRef](#)]

56. Meligrana, G.; Ferrari, S.; Lucherini, L.; Celè, J.; Colò, F.; Brugger, J.; Ricciardi, C.; Ruffo, R.; Gerbaldi, C. Na₃V₂(PO₄)₃-Supported Electrospun Carbon Nanofiber Nonwoven Fabric as Self-Standing Na-Ion Cell Cathode. *ChemElectroChem* **2020**, *7*, 1652–1659. [[CrossRef](#)]
57. Vu, A.; Qian, Y.; Stein, A. Porous Electrode Materials for Lithium-Ion Batteries—How to Prepare Them and What Makes Them Special. *Adv. Energy Mater.* **2012**, *2*, 1056–1085. [[CrossRef](#)]
58. Kalluri, S.; Seng, K.H.; Guo, Z.; Liu, H.K.; Dou, S.X. Electrospun Lithium Metal Oxide Cathode Materials for Lithium-Ion Batteries. *RSC Adv.* **2013**, *3*, 25576–25601. [[CrossRef](#)]
59. Rangan, K.K.; Gopalakrishnan, J. AMVMIII(PO₄)₃: New Mixed-Metal Phosphates Having NASICON and Related Structures. *Inorg. Chem.* **1995**, *34*, 1969–1972. [[CrossRef](#)]
60. Patoux, S.; Rouse, G.; Leriche, J.-B.; Masquelier, C. Structural and Electrochemical Studies of Rhombohedral Na₂TiM(PO₄)₃ and Li_{1.6}Na_{0.4}TiM(PO₄)₃ (M = Fe, Cr) Phosphates. *Chem. Mater.* **2003**, *15*, 2084–2093. [[CrossRef](#)]
61. Hung, T.-F.; Lan, W.-H.; Yeh, Y.-W.; Chang, W.-S.; Yang, C.-C.; Lin, J.-C. Hydrothermal Synthesis of Sodium Titanium Phosphate Nanoparticles as Efficient Anode Materials for Aqueous Sodium-Ion Batteries. *ACS Sustain. Chem. Eng.* **2016**, *4*, 7074–7079. [[CrossRef](#)]
62. Ferrari, A.C.; Robertson, J. Interpretation of Raman Spectra of Disordered and Amorphous Carbon. *Phys. Rev. B* **2000**, *61*, 14095–14107. [[CrossRef](#)]
63. Bachtin, K.; Kramer, D.; Chakravadhanula, V.S.K.; Mu, X.; Trouillet, V.; Kaus, M.; Indris, S.; Ehrenberg, H.; Roth, C. Activation and Degradation of Electrospun LiFePO₄ Battery Cathodes. *J. Power Sources* **2018**, *396*, 386–394. [[CrossRef](#)]
64. Liu, Y.; Rong, X.; Zhao, J. Unlocking the Multi-Electron Transfer Reaction in NASICON-Type Cathode Materials. *Mater. Futures* **2023**, *2*, 023502. [[CrossRef](#)]
65. Hu, Y.; Wu, L.; Liao, G.; Yang, Y.; Ye, F.; Chen, J.; Zhu, X.; Zhong, S. Electrospinning Synthesis of Na₂MnPO₄F/C Nanofibers as a High Voltage Cathode Material for Na-Ion Batteries. *Ceram. Int.* **2018**, *44*, 17577–17584. [[CrossRef](#)]
66. Xiang, J.; Dong, D.; Wen, F.; Zhao, J.; Zhang, X.; Wang, L.; Liu, Z. Microwave Synthesized Self-Standing Electrode of MoS₂ Nanosheets Assembled on Graphene Foam for High-Performance Li-Ion and Na-Ion Batteries. *J. Alloys Compd.* **2016**, *660*, 11–16. [[CrossRef](#)]
67. Bruker AXS. *General Profile and Structural Analysis Software for Powder Diffraction Data, TOPAS V3.0*; User Manual Bruker AXS: Karlsruhe, Germany, 2005.

Disclaimer/Publisher's Note: The statements, opinions and data contained in all publications are solely those of the individual author(s) and contributor(s) and not of MDPI and/or the editor(s). MDPI and/or the editor(s) disclaim responsibility for any injury to people or property resulting from any ideas, methods, instructions or products referred to in the content.